Comparison of two hot tearing criteria in numerical modelling of arc welding of stainless steel AISI 321

Michel Bellet, Gonghao Qiu, Jean-Michel Carpreau

▶ **To cite this version:**

Michel Bellet, Gonghao Qiu, Jean-Michel Carpreau. Comparison of two hot tearing criteria in numerical modelling of arc welding of stainless steel AISI 321. Journal of Materials Processing Technology, 2016, 230, pp.143-152. 10.1016/j.jmatprotec.2015.11.002 . hal-01253132

HAL Id: hal-01253132

https://minesparis-psl.hal.science/hal-01253132

Submitted on 3 Jan 2017

HAL is a multi-disciplinary open access archive for the deposit and dissemination of scientific research documents, whether they are published or not. The documents may come from teaching and research institutions in France or abroad, or from public or private research centers.

L'archive ouverte pluridisciplinaire **HAL**, est destinée au dépôt et à la diffusion de documents scientifiques de niveau recherche, publiés ou non, émanant des établissements d'enseignement et de recherche français ou étrangers, des laboratoires publics ou privés.

Journal of Materials Processing Technology 230 (2016) 143-152
http://dx.doi.org/10.1016/j.jmatprotec.2015.11.002

COMPARISON OF TWO HOT TEARING CRITERIA IN NUMERICAL MODELLING OF ARC WELDING OF STAINLESS STEEL AISI 321

Michel Bellet[1], Gonghao Qiu[2], Jean-Michel Carpreau[3]

1 MINES ParisTech, PSL Research University, CEMEF – Centre de mise en forme des matériaux, CNRS UMR 7635, Sophia Antipolis, France, michel.bellet@mines-paristech.fr

2 EDF CEIDRE, Saint-Denis, France, gonghao.qiu@edf.fr

3 LaMSID UMR EDF-CNRS-CEA 2832, Clamart, France, jean-michel.carpreau@edf.fr

Corresponding author: Michel Bellet

Abstract —Two hot cracking criteria have been tested: the RDG criterion, based on the prediction of liquid cavitation as a precursor of crack formation, and a strain-based solid mechanics criterion. Both criteria have been implemented in a finite element thermo-mechanical simulation of gas tungsten arc welding. After comparison with experimental results obtained in a test campaign on stainless steel AISI 321, both criteria have shown good ability to predict crack occurrence. Yet, the best response in terms of cracking prediction was obtained with the strain-based solid mechanics criterion.

Keywords — Welding, Hot cracking, Hot tearing, Solidification cracking, Numerical modelling, Hot cracking criteria

INTRODUCTION

Hot cracking is a common defect occurring during solidification and welding of metallic alloys. In industrial welding practice, a lot of prototype tests are realized to define operating

parameters (welding heat input, chemical composition) in order to avoid hot cracking. Such tests are expansive and time consuming. In addition, as they do not cover all real industrial welding configurations, they do not guarantee absence of cracking. Alternatively, it might be expected that the progress in the numerical modelling of welding processes could be used in hot cracking sensitivity prediction. The aim of this contribution is to study the capacity of two hot cracking criteria to predict such a defect. In a first section, we will proceed to a brief reminder of what is hot cracking and what are the main physical phenomena involved. The two main classes of hot cracking criteria that can be found in the literature will be introduced. In a second part, the main equations governing the thermomechanical analysis of welding will be presented. A third section will present the experimental results obtained by GTA (gas tungsten arc) welding on rectangular plates of stainless steel AISI 321. The numerical thermal analysis of those tests will be discussed in a fourth section, showing the accurate calibration of the thermal model with respect to experimental records. Then, the thermomechanical analysis will be presented and finally the response of the two types of hot cracking criteria will be analyzed and discussed.

1 Hot cracking and prediction criteria

Hot cracking (also named hot tearing or solidification cracking) is a well-known welding defect occurring at the end of solidification. Readers can refer to Campbell (2003) which gave a comprehensive and synthetic description of this defect in his book on castings. During solidification, low melting point liquid exists between dendrites. At the end of solidification (high solid fraction) the stresses initiated by solidification shrinkage or by thermal gradients in the surrounding solid may be sufficient to open interdendritic spaces not yet completely solidified and create intergranular cracks that liquid feeding cannot fill. Among many authors, Eskin and Katgerman (2007) studied and established a comprehensive review of the different

physical phenomena leading to this defect. Alloys are considered the most vulnerable in the so-called Brittleness Temperature Range (BTR). This temperature interval - the name of which expresses that hot cracking may be seen as a ductility loss - is between the coherency and the coalescence temperature. The coherency temperature can be defined when dendrites begin to transmit forces but with low rigidity. Above coherency temperature, any deformation or displacement of solid dendrites can be easily compensated by the circulating liquid phase. The coalescence temperature is reached when dendrites are strong enough to accommodate strain, while numerous solid bridges limit the risk of crack propagation. In between these characteristic temperatures – or equivalently characteristic solid fractions – that is when liquid cannot flow any more through interdendritic spaces, the mushy zone is susceptible to hot cracking. Farup et al. (2001) provided spectacular evidences of the combination of phenomena leading to hot cracking: liquid cavitation, lack of liquid feeding, and plastic deformation of solid bridges.

From the previous considerations, it can be deduced that a given alloy will be more or less prone to solidification cracking depending on its thermophysical and rheological properties and on local specific solidification conditions determining for instance dendritic spacing and, as a consequence, mushy zone permeability. In addition, Cross and Coniglio (2008) showed like other researchers the existence of a critical strain, below which no solidification crack occurs, and the influence of strain-rate. Regarding the prediction of hot cracking, models can be grouped into two great families that are presented in the next two sections.

1.1 Liquid cavitation approach: RDG criterion

The so-called RDG criterion (so-called from the initials of their authors) was proposed by Rappaz et al. (1999). The authors considered the mass balance between solidification shrinkage and liquid feeding through the permeable solid dendritic network. Hot tearing was

supposed to occur due to a deficit of liquid feeding through the mushy zone, leading to cavitation in the interdendritic liquid, and then to crack initiation. Assuming a thermal gradient oriented along *x* direction, also the direction of columnar dendritic growth, the mass balance equation was approached as

$$(1+\beta)(\dot{\varepsilon}_{yy}+\dot{\varepsilon}_{zz})\,f_s+\beta\frac{\partial f_s}{\partial t}=\frac{\partial}{\partial x}\left(\frac{\mathrm{K}}{\mu}\left(\frac{\partial p}{\partial x}-\rho_l g_x\right)\right) \tag{1}$$

where $\beta=\rho_s/\rho_l-1$ is the solidification shrinkage coefficient, f_s is the solid fraction, $\dot{\varepsilon}_{yy}$ and $\dot{\varepsilon}_{zz}$ are solid strain rate components perpendicular to the growth direction. The two terms summed in the left hand side of Eq. (1) are associated with the mechanical deformation and the solidification shrinkage, respectively. The deformation parallel to the dendrites was ignored, as it could not induce hot tearing, and the densities of the two phases, liquid and solid, were assumed constant. The right hand side term expresses the liquid feeding governed by Darcy law, where K is the permeability, μ the liquid viscosity and *p* the liquid pressure.

The permeability K may be expressed by the Carman-Kozeny equation:

$$\mathrm{K}=\lambda_2{}^2\frac{(1-f_s)^3}{180\,f_s{}^2} \tag{2}$$

in which λ_2 denotes the secondary dendrite arm spacing (SDAS). This value is often determined experimentally by metallurgical expertise. It increases with solidification time (the time spent in the solidification interval) by dendrites maturing. This phenomenon, which is due to the diffusion of atoms from high to low curvature zones in order to minimize the chemical potential, decreases the number of secondary branches and thus increases the interdendritic space. This explains why the distance between dendrites depends strongly on the cooling rate. The SDAS can be estimated by power law type expressions as a function of the solidification time t_f, such as introduced by Kurz and Fisher (1986):

$$\lambda_2 = M t_f^{1/3} \tag{3}$$

where M is a material constant.

Rappaz et al. (1999) proceeded to the integration of the mass balance equation along the length of the mushy zone, which lead to a relationship between the tensile strain rate $\dot{\varepsilon}$ applied perpendicular to the solidification direction on one hand, and the liquid pressure drop through the mushy zone $\Delta p = p_m - p$ on the other hand, p_m denoting the metallostatic pressure in the liquid pool, at dendrite tips. The liquid pressure p continuously decreases in the mushy zone, from the tips to the roots of primary columnar dendrites. Close to dendrite roots, that is below the coalescence temperature, near the full solid region, the liquid pressure may reach the cavitation pressure. The comparison of this pressure drop to its critical value $\Delta p_{crit} = p_m - p_C$, where p_C is the cavitation pressure, leads to a critical strain rate $\dot{\varepsilon}$. According to Rappaz et al., hot cracking was then supposed to initiate when:

$$\dot{\varepsilon} > \frac{G}{B}\left[\frac{G\lambda_2^{\,2}}{180\mu(1+\beta)}\Delta p_{crit} - v_T\frac{\beta}{(1+\beta)}A\right] \tag{4}$$

where G is the norm of the temperature gradient in the mushy zone, v_T is the speed of the solidification front, A and B are integrals that depend on the solidification path of the alloy, the bounds of the integrals hereunder being the bounds of the BTR, upper bound T_{coh}, lower bound T_{coal}:

$$A = \int_{T_{coal}}^{T_{coh}} \frac{f_s^{\,2}}{(1-f_s)^2}\,dT \qquad B = \int_{T_{coal}}^{T_{coh}} \frac{f_s^{\,2}}{(1-f_s)^3}\left(\int_{T_{coal}}^{T} f_s\,dT\right)dT \tag{5}$$

In the context of welding, note that the metallostatic pressure can be neglected, so that $\Delta p_{crit} = -p_C$. It can be seen that using this model, the critical strain rate can be determined by

thermal analysis. A central parameter for the application of the RDG criterion is the liquid cavitation pressure, corresponding to the critical cavity size leading to hot cracking.

1.2 Mechanical approach: strain-based criteria

In mechanical criteria, the physical phenomena associated with cracking are not explicitly described. Such models are based on a mechanical load limit, which is generally expressed in terms of a critical strain cumulated through the BTR. Below this limit, welding is assumed to be free from hot cracking. In practice, the Hot Cracking susceptibility Index (HCI) is often considered and is expressed as the difference between the cumulated strain $\bar{\varepsilon}_{BTR}$ in the brittle temperature range and a reference value ε_{crit}. Yamanaka (1990) was the first one to express such a simple mechanical criterion:

$$HCI = \bar{\varepsilon}_{BTR} - \varepsilon_{crit} \quad \text{with} \quad \bar{\varepsilon}_{BTR} = \int_{BTR} \dot{\bar{\varepsilon}} \mathrm{d}t \tag{6}$$

Hence, positive values of HCI indicate hot cracking risk. In the summation, $\dot{\bar{\varepsilon}}$ denotes a scalar measure of the strain rate components in the direction perpendicular to the thermal gradient. Generally, compressive strain rate components are not taken into account because they do not have significant effect on hot cracking. This is why Bellet et al. (2009) proposed two different expressions for this measure (von Mises type or largest positive eigen value). Note that these remarks also apply to Eq. (4) when using the RDG criterion.

It can be seen from Eq. (6) that, using this simple approach, the associated criterion has only three parameters which are on one hand the upper and lower limits of the BTR, expressed in terms of temperature or corresponding solid fraction, and on the other hand the strain limit ε_{crit}.

Won et al. (2000) proposed another mechanical criterion, which is an extension of the previous one and includes strain-rate influence. It is expressed as follows, the critical strain ε_{crit} being expressed as a function of the strain rate itself and of the BTR:

$$\varepsilon_{crit} = \frac{\varphi}{\dot{\bar{\varepsilon}}^{m} BTR^{n}} \tag{7}$$

Here φ, n and m are material constants, extending the number of parameters to 5.

Based on the work of Won et al., Bellet et al. (2009) proposed to express the critical strain as a function of the chemical concentration of specific elements to reflect the increase in the solidification range with segregation together with the influence of such chemical elements on phenomena such as wetting of the solid phase by the liquid phase, that is known to impact the sensitivity to hot tearing. The parameter φ now depends itself on the mass concentration of carbon, manganese, sulphur and phosphorus:

$$\varphi = \varphi_0 \Big/ \left(a_0 \exp(b_0[\mathrm{C}]) \left(\frac{[\mathrm{Mn}]}{[\mathrm{S}]} \right)^{c_0} [\mathrm{P}]^{d_0} \right) \tag{8}$$

This involves again additional material parameters: 9 in total.

In the present study, the analysis is restricted to the choice of the simplest mechanical criterion, the one of Yamanaka et al., because of its limited number of parameters. The use of alternative criteria would have required a more extended experimental data base, which was out the scope of this work.

2 Experimental results

The studied steel is a stainless steel, grade AISI 321 (titanium stabilized austenitic stainless steel), the chemical composition of which is indicated in Table 1. The values of

thermo-physical properties and constitutive parameters can be found in (Kerrouault, 2000) who carried out various studies on welding of this steel grade.

Table 1: Measured chemical composition of steel AISI 321 (weight%).

C	Si	Mn	P	Cr	Ni	Ti	S	N
0.029	0.46	0.94	0.0.21	17.15	9.02	0.310	<0.01	0.011

Several types of hot cracking tests in welding conditions have been developed in the past, essentially consisting of a straight welding line performed on a plate, in order to create a possible axial crack in the wake of the welding torch. Tests differ by the plate geometry and boundary conditions. The hot cracking test considered here is of rectangular shape, as in the work of Shibahara et al. (2001) who developed this test in the Joining and Welding Research Institute in Osaka. In the literature, this hot cracking test tends to be named JWRI test. It consists of a straight TIG (GTA) weld bead on a flat rectangular plate specimen (length 140 mm, thickness 2 mm, width 20, 25 and 40 mm), which is clamped at one end (Figure 1). The other end is free. Through-thickness welding is started at 5 mm from this free end and is done without any filler material, so that the weld bead in question is in fact a simple straight fusion line, as indicated on the figure. At the beginning of the test, the fusion zone passes through the width reduction (notch in the coupon). At this moment the 25 mm long appendix detaches while an overheated zone and an enlarged fusion zone are generated temporarily, which favors the initiation of an axial crack. Then, depending on welding conditions, either the crack stops immediately or it progresses in the axial direction in the wake of the torch, up to the end of welding. Such an axial crack is shown in Figure 1c. The test is then discriminant between cracked and non-cracked specimens which will be denoted hereafter "C" and "NC" respectively. Protection against oxidation is assured by argon gas on the upper side of the plate and by disposal of very thin copper foils maintained by adhesives along the lower face of the

plate (Figure 1b).

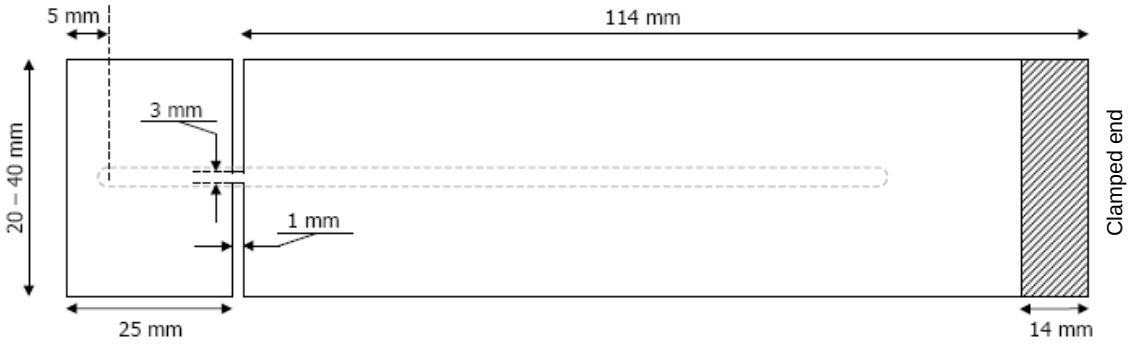

a)

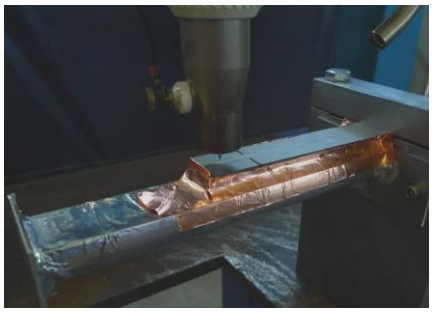

b)

c)

Figure 1: Hot cracking test: a) geometry of plate specimens ; b) experimental set-up showing clamping and protection against oxidation on the lower side of the plate ; c) example of a crack fully developed throughout the weld bead (test 4 of Table 2).

Six process conditions, corresponding to different welding parameters and plate geometry have been tested, as detailed in Table 2. Welding arc voltage is 10 V and welding heat input (energy) is about 235 J/mm, with variable arc current, welding speed and coupon width. The occurrence of a crack is indicated in the last column of the table. When crack is started through a notch at the coupon edge, like with this kind of specimen, the closure or continuation of the crack is often correlated with the coupon width. Cross and Boellinghaus (2006) analyzed this relation and showed the influence of the coupon width on the amplitude of transverse tensile stress and strain, leading to cracking. However, in the present case, it can be seen that there is no direct apparent relation between crack occurrence and one of the operating or geometrical parameters: coupon width, arc current, welding speed or heat input.

Note that in test 2, a crack formed but stopped after 30 mm propagation; this is the reason for the indication "C-NC".

Table 2: Welding test configurations.

Test #	Coupon width [mm]	Arc voltage *U* [V]	Arc current *I* [A]	Welding speed *V* [mm/s]	Welding heat input (*UI*/*V*) [J/mm]	Result: crack / no-crack
1	20	10	109	4.67	233.6	C
2	20	10	102	4.33	235.4	C-NC
3	25	10	102	4.33	235.4	NC
4	25	10	109	4.67	233.6	C
5	40	10	109	4.67	233.6	NC
6	40	10	117	5.00	234.0	NC

Metallurgical investigations by scanning electronic microscopy (SEM, Figure 2) demonstrate that cracks are interdendritic, confirming a hot cracking mechanism. At the bottom of a section perpendicular to the welding direction, dendrites are found to grow perpendicular to the lower face of the specimen, that is perpendicular to isothermal surfaces that are parallel to this face. At mid-thickness the dendritic growth direction is out of the observation plane, which is consistent with the fact that the temperature gradient tends to align itself along the welding direction at the rear of the welding pool. From the observations, the secondary dendrite arm spacing can be estimated between 4 and 7 µm. Micro-probe analysis has not detected any sulphur or phosphorus segregation.

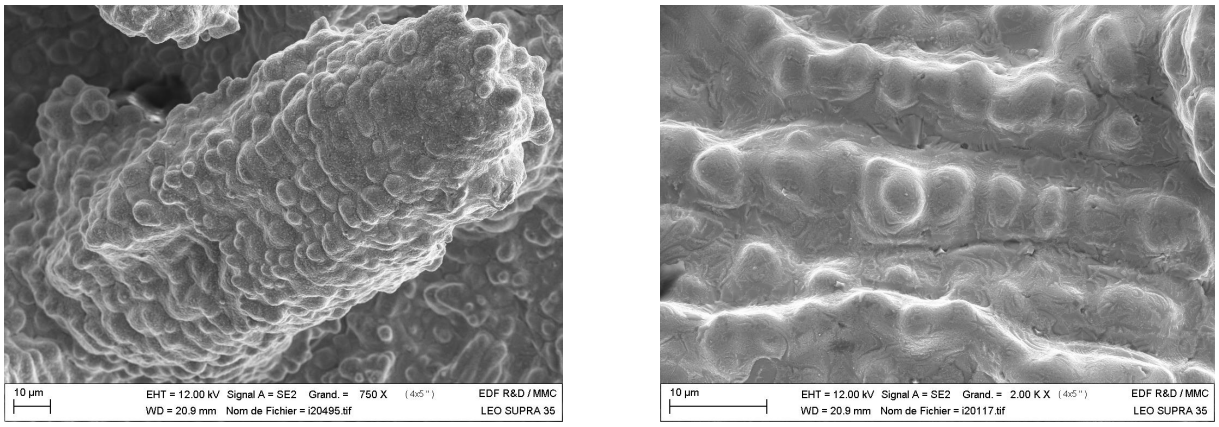

Figure 2: SEM observation of primary (left) and secondary (right) dendrites in the crack propagation zone.

3 Numerical modelling

The numerical simulation consists of a non-steady-state thermal-mechanical finite element calculation, which is performed in two separate steps. First, the evolution of the temperature field is calculated. Second, this time dependent temperature distribution is used on the same finite element mesh in a mechanical resolution to determine stress and strain fields. The numerical code used to solve the non-linear equations for energy and momentum conservation is the open source code Code_Aster (2015).

The numerical simulation is not supposed to address the high complexity of the transient start of the weld especially when passing through the width reduction (notch) initiating cracks. The objective is limited here to the non-steady state modelling of the thermomechanical conditions undergone at the rear of the fusion zone once a quasi-steady state regime has been established in the plate.

The finite element meshes are composed of hexahedral and tetrahedral elements with linear interpolation, integrated with 8 and 6 Gauss points, respectively. The mesh size is coarser in the base metal, far from the welding direction (3 mm) and refined in the region of interest, that is at the rear of the mushy zone around *x*-locations along the welding line where crack occurrence has been experimentally observed (mesh size decreased up to 190 (*x*) x 220 (*y*) x 400 (*z*) µm). An illustration is given Figure 3. The mesh covers the zone of interest in the

specimen for potential crack formation: the domain between the notch and the clamping zone (100 mm in length). The clamped region of the plate is not modelled: the displacement of the nodes at the end of the mesh is imposed to be null. In the two next sections, the main assumptions of the non-steady-state thermal-mechanical calculations are listed and the governing equations are presented.

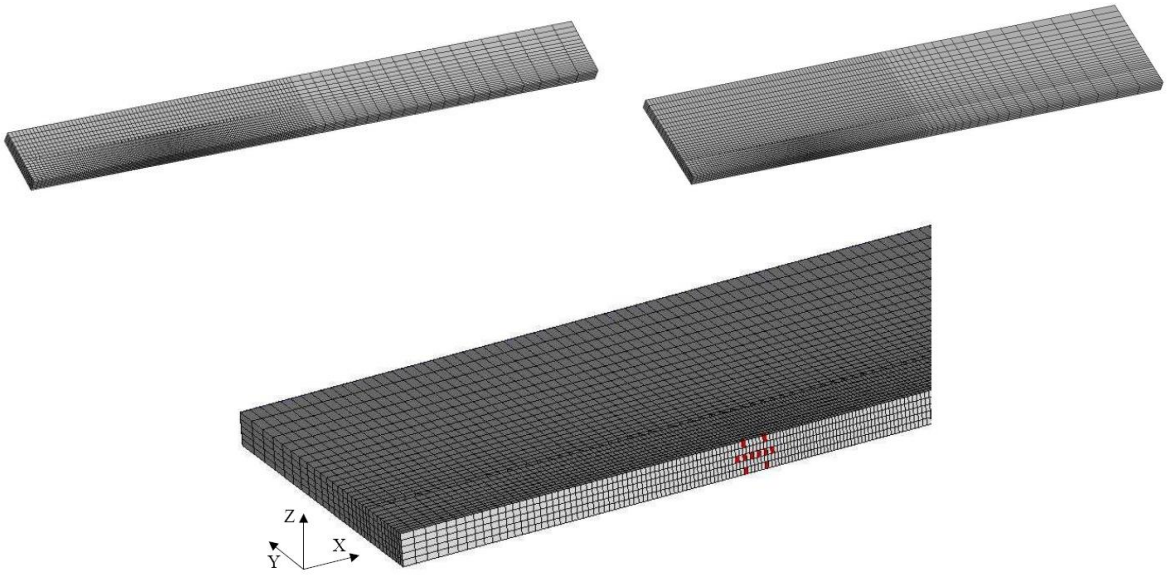

Figure 3: Finite element meshes for coupons of width 20 and 40 mm (top). The bottom picture shows a zoom in the refined region.

3.1 Assumptions

The main assumptions are:

1. The transient welding process is treated by an equivalent thermal loading. There is neither plasma nor welding pool flow modelling.

2. The mechanical behaviour of the material is modelled on the whole temperature range using an elastic-viscoplastic constitutive law. Material properties are temperature dependent and adapted over solidus temperature to reflect the decrease in strength up to a given coherency temperature, over which strain and stress are considered null.

3. Solidification shrinkage is ignored, as it is supposed to essentially affect liquid flow, which is disregarded in the present modelling approach.
4. Energy associated with plastic deformation is ignored, due to very low strain rates, making it insignificant in front of heat sources arising from the welding process.
5. Chemical segregation due to solidification, fluid flow or diffusion in the solid state is ignored. The solidification path is given by the Gulliver-Scheil equation.

3.2 Governing equations

The equation for energy conservation is:

$$\frac{\partial H}{\partial t} - \nabla \cdot (k \nabla T) = q \tag{9}$$

in which k is the thermal conductivity and H the enthalpy per unit of volume:

$$H(T) = \int_{T_0}^{T} \rho c_p(u) du \tag{10}$$

ρ denotes the density, c_p the specific heat and T_0 a reference temperature. The right hand side scalar q in Eq. (9) denotes the local heat input per unit of volume, which is associated with the welding process and will be detailed in the next section.

The thermal boundary condition applied to all faces of the welded plate consists of a mixed convection-radiation condition, for which the heat flux is defined as:

$$-k \nabla T \cdot \mathbf{n} = h_c (T - T_{air}) + \varepsilon_r \sigma_r (T^4 - T_{air}^4) \tag{11}$$

where h_c is the convective heat transfer coefficient, σ_r the Stefan-Boltzmann constant, ε_r the material emissivity, T_{air} the temperature of surrounding air, and **n** the unit outward normal vector.

The equation for momentum conservation is:

$$\nabla \cdot \boldsymbol{\sigma} + \mathbf{f} = 0 \tag{12}$$

in which inertia effects are neglected, **f** is the body force per unit of volume and $\boldsymbol{\sigma}$ is the Cauchy stress tensor. The deviatoric stress tensor and the von Mises equivalent stress are respectively defined as:

$$\boldsymbol{\sigma}^{dev} = \boldsymbol{\sigma} - \frac{1}{3}\mathrm{tr}(\boldsymbol{\sigma})\mathbf{I} \qquad \bar{\sigma} = \sqrt{\frac{3}{2}\boldsymbol{\sigma}^{dev} : \boldsymbol{\sigma}^{dev}} \tag{13}$$

where **I** is the identity tensor. The strain rate is divided into three components, elastic, thermal and viscoplastic as:

$$\dot{\boldsymbol{\varepsilon}} = \dot{\boldsymbol{\varepsilon}}^{el} + \dot{\boldsymbol{\varepsilon}}^{vp} + \dot{\boldsymbol{\varepsilon}}^{th} \tag{14}$$

In the framework of small elastic strains, the material being assumed isotropic, the elastic strain rate tensor $\dot{\boldsymbol{\varepsilon}}^{el}$ and the thermal strain rate tensor $\dot{\boldsymbol{\varepsilon}}^{th}$ are respectively given by:

$$\dot{\boldsymbol{\varepsilon}}^{el} = \frac{1+\nu}{E}\dot{\boldsymbol{\sigma}} - \frac{\nu}{E}\mathrm{tr}(\dot{\boldsymbol{\sigma}})\mathbf{I} \qquad \dot{\boldsymbol{\varepsilon}}^{th} = \alpha\frac{\mathrm{d}T}{\mathrm{d}t}\mathbf{I} \tag{15}$$

where E is the Young modulus, ν the Poisson coefficient, and α the one-dimensional thermal expansion coefficient. The viscoplastic strain rate is expressed by means of a viscoplastic law including kinematic hardening. Denoting *F* the plasticity criterion and *R* the yield stress, we have:

$$F(\boldsymbol{\sigma}, \mathbf{X}) = \overline{(\boldsymbol{\sigma} - \mathbf{X})} - R = \sqrt{\frac{3}{2}(\boldsymbol{\sigma} - \mathbf{X})^{dev} : (\boldsymbol{\sigma} - \mathbf{X})^{dev}} - R \tag{16}$$

where *R* is supposed, in the present study, to depend on temperature only. The tensor **X** is the kinematic hardening stress tensor, whose expression is given hereunder. The viscoplastic

strain rate tensor is then expressed by

$$\dot{\boldsymbol{\varepsilon}}^{vp} = \dot{\lambda}\frac{\partial F}{\partial \boldsymbol{\sigma}} = \frac{3}{2}\frac{\dot{\lambda}}{\overline{(\boldsymbol{\sigma}-\mathbf{X})}}(\boldsymbol{\sigma}-\mathbf{X})^{dev} \tag{17}$$

from which it can easily be shown that the multiplier $\dot{\lambda}$ is simply the generalized viscoplastic strain rate $\dot{\bar{\varepsilon}}$:

$$\dot{\lambda} = \dot{\bar{\varepsilon}} = \sqrt{\frac{2}{3}\dot{\boldsymbol{\varepsilon}}^{vp} : \dot{\boldsymbol{\varepsilon}}^{vp}} \tag{18}$$

The kinematic hardening tensor **X** is given by

$$\mathbf{X} = \frac{2}{3}C\boldsymbol{\alpha} \qquad \text{with} \qquad \dot{\boldsymbol{\alpha}} = \dot{\boldsymbol{\varepsilon}}^{vp} - \gamma\dot{\bar{\varepsilon}}\boldsymbol{\alpha} \tag{19}$$

where C and γ are material parameters. Note that **X** is a deviatoric tensor. Finally, the viscous flow is described by a power law:

$$\dot{\bar{\varepsilon}} = \left(\frac{\langle F\rangle}{K}\right)^{n} \tag{20}$$

in which the Macauley bracket $\langle\cdot\rangle$ expresses that there is a non-zero viscoplastic strain rate only if F is positive: $\langle F\rangle = F$ if $F > 0; \langle F\rangle = 0$ otherwise. In total, the mechanical constitutive model has seven material parameters, possibly temperature dependent: E, ν, R, C, γ, K, and n. All parameter values for the considered steel AISI 321 can be found in (Kerrouault, 2000), together with its thermophysical properties.

4 Thermal analysis

The heat source term associated with the welding process and appearing as the right hand side of the heat equation (Eq. (9)) is:

$$q(x,y,z,t) = \frac{3\eta UI}{\pi æ r_b^{\,2}} \exp\left[-\frac{(x-Vt)^2 + y^2 + f_p(e-z)^2}{r_b^{\,2}} \right] \mathrm{H}(z+s) \qquad (21)$$

where x is the spatial coordinate in the welding direction (y in the transverse direction and z in the thickness direction), U and I are respectively the arc voltage and current, η a process efficiency parameter, V the welding speed, e the plate thickness, r_b the characteristic radius of the arc source, f_p and s are factors defining the attenuation of q in the thickness direction z, H being the Heaviside function.

The convective heat transfer coefficient h_c has been taken equal to 15 W m^{-2} K^{-1}. Other parameters such as the thermal emissivity ε_r and the heat source parameters (η, r_b, f_p and s) have been identified by an inverse method, which consists in minimizing the difference between measured temperatures with thermocouples and calculated temperatures calculated by the finite element method. Details can be found in Qiu (2010) who proceeded to this minimization by coupling the software Code_Aster and Matlab. The maximum difference between measured and simulated temperatures after optimization is 30 °C (Figure 4), which is acceptable in consideration of thermal gradients near mushy zone of the order of 50 °C/mm. Moreover, weld pool size and shape have been compared. Experimental depth and half-width are measured on post-mortem metallographic transverse sections, such as the one shown Figure 5. The calculated dimensions are determined by the isothermal surface corresponding to the liquidus temperature (1440 °C). As shown in the figure, the relative difference between calculated (1.62 mm) and observed (1.71 mm) half-width is 5 %. As regards pool depth, the difference is 14 % (calculated 0.72 mm, measured 0.84 mm). Similar results have been obtained for the different welding conditions. It can be concluded that the thermal calculation

is representative of the reality of the welding process, and therefore can be used as a sound basis for thermal-mechanical calculations.

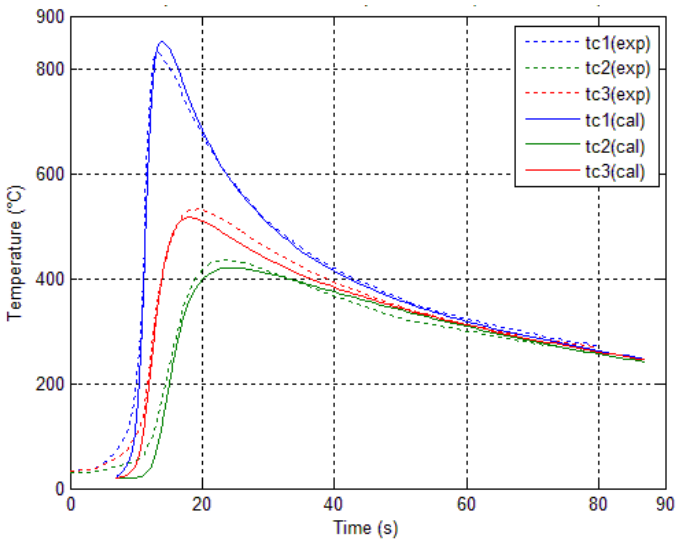

Figure 4: Comparison between simulated and measured temperature evolutions for test 2 (coupon width 20 mm, arc voltage 10 V, arc current 102 A, welding speed 4.33 mm/s). Thermocouples 1, 2 and 3 are welded on the upper face of the sheet, at a lateral distance of 5, 12 and 10 mm from the welding line, respectively.

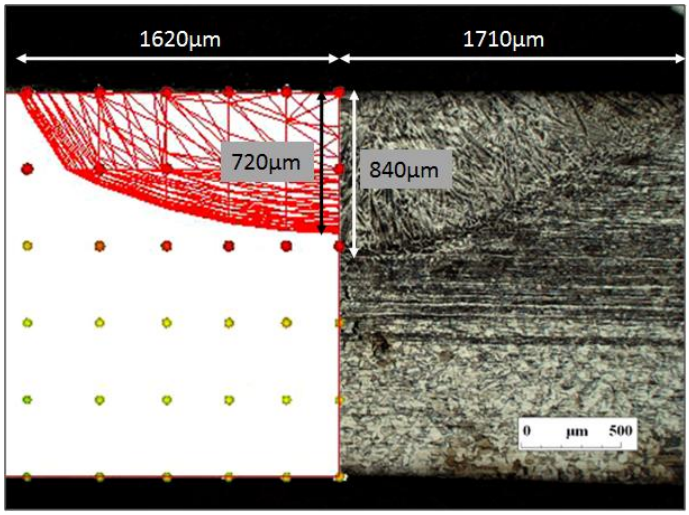

Figure 5: Comparison between simulated and measured weld pool size (test 2).

Non steady-state thermal calculations also show that the size of the fully molten zone (T > 1440 °C) becomes constant from the first few seconds. The convergence of the transient solution to a steady state is established in less than 6 seconds and this steady state situation is

illustrated in Figure 6 in which the temperature field is plotted in the vicinity of the fusion zone.

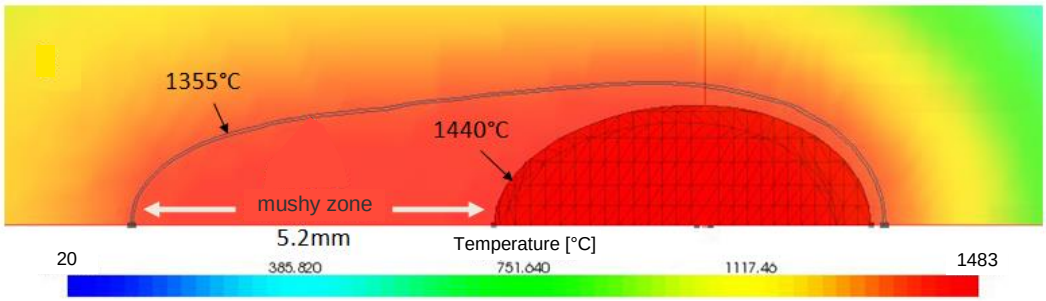

Figure 6: Representation of the calculated mushy zone and liquid weld pool for test 3 (coupon width 25 mm, arc voltage 10 V, arc current 102 A, welding speed 4.33 mm/s) after a steady state has been reached in the transient resolution. 1355 °C is the solidus temperature and 1440 °C is the liquidus temperature.

5 Mechanical analysis

Figure 7 shows the distribution of transverse stress σ_{yy} after a quasi-steady state regime is obtained in the non-steady-state calculation, that is after 6 s. It can be seen that with respect to the weld pool, the upstream zone undergoes a slight traction, while a more marked compression (280 MPa) prevails closer to the pool. The stress is null for temperatures above the liquidus temperature. At the rear of the weld pool, where solidification ends, tensile transverse stress can be seen. Tensile stress in the mushy zone would possibly lead to cracking by opening axial longitudinal cracks, as observed on the cracked specimens. When the material is completely solidified, the tensile stress continues to grow but the risk of cracking is much smaller because the structure has already coalesced or is fully solid and can sustain such internal stresses. The lower part of Figure 7 illustrates the corresponding variation of the transverse stress at a location fixed and belonging to the weld center line. The transverse stress is plotted against temperature, showing the successive transverse stress undergone by the material during welding.

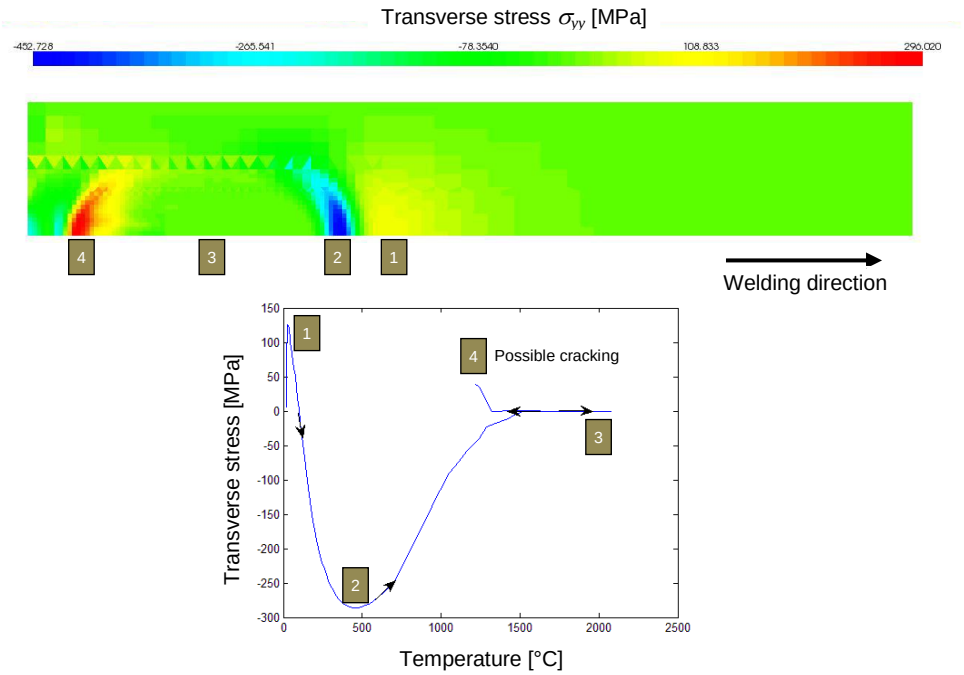

Figure 7: Distribution of transverse stress around the weld pool, in steady state regime (top) and variation of this stress component with temperature for a material point located on the weld center line (bottom), in the case of test 3 of Table 2. Brown labels indicate the successive states of a material point.

6 Model results and discussion

All six tests described in Table 2 have been subject to thermal-mechanical simulation. In the present section we present and discuss the performance of the two hot cracking criteria, in comparison with the experimental occurrence of cracks in the specimens.

6.1 Interpretation through the mechanical criterion

The coherency temperature of the alloy (which is generally supposed as being the upper bound of the BTR) is chosen as T_{coh} = 1400 °C, corresponding to a solid fraction f_s = 0.8. First, we examine the build-up of stress below this coherency temperature, as shown Figure 8. In this figure, for each welding test the transverse stress component σ_{yy} is plotted for a material point located on the weld center line in the region of interest during the crossing of the lower part of the solidification interval, below T_{coh}. Clearly, calculated stress levels do not correlate with the cracking status (C or NC) of specimens during tests. It is worth noting that

this result is contrary to stress-based hot tearing criteria, such as the one proposed by Lahaie and Bouchard (2001) who derived a stress limit deduced from the stress necessary to separate plates bonded by capillary force. Conversely, in the following paragraph, it will be shown that strain levels indeed correlate much better with cracking status.

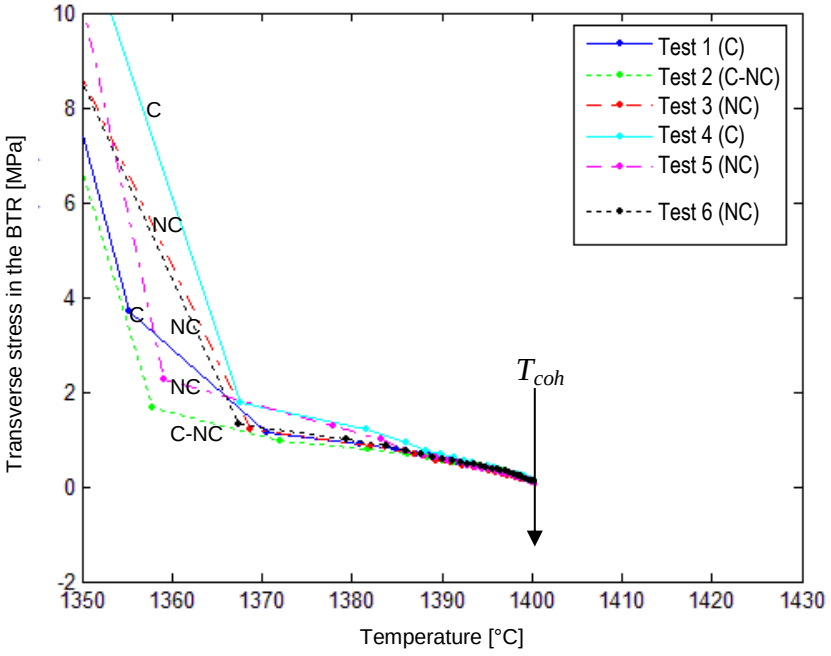

Figure 8: Calculated transverse stress σ_{yy} as a function of temperature during the stress build-up below the coherency temperature (1400 °C, f_s = 0.8) for the six tests studied.

Figure 9 presents the calculated cumulated plastic strain between temperature T_{coh} and the solidus temperature (1355 °C), for a material point at the rear of the weld pool, and for the six cases studied. As mentioned above, the cumulated plastic strain results from a time integration of the highest tensile component of the strain-rate tensor (here the $\dot{\varepsilon}_{yy}$ component) while the material point is found between coherency and solidus temperatures. Unlike stress levels, it can be seen that the highest cumulated strains are found for the specimens in which effective cracking is observed. The agreement with experimental findings is much better than when considering stress levels. In addition, and in the perspective of expressing the criterion by use of a cumulated deformation on the BTR [T_{coal}, T_{coh}], it is interesting to notice that the

choice of the lower bound for the BTR – the coalescence temperature – close to solidus temperature, appears not to be crucial, as there is no marked strain increase near solidus. However, due to the fact that the value of the solidus temperature is generally difficult to determine experimentally and that liquid fraction changes slowly with temperature near solidus, it might be recommended to fix the lower bound at a solid fraction of 0.95. That would correspond for the considered alloy to a temperature of 1360 °C.

From Figure 9 it can be seen that the cumulated strain for cracking specimens is higher than 0.02, while it is lower than 0.015 for non-cracking specimens. Therefore a critical plastic strain of 1.5 % in a BTR ranging from 1400 °C (f_s = 0.8) to 1360 °C (f_s = 0.95) or to the solidus could be recommended to estimate a risk of cracking.

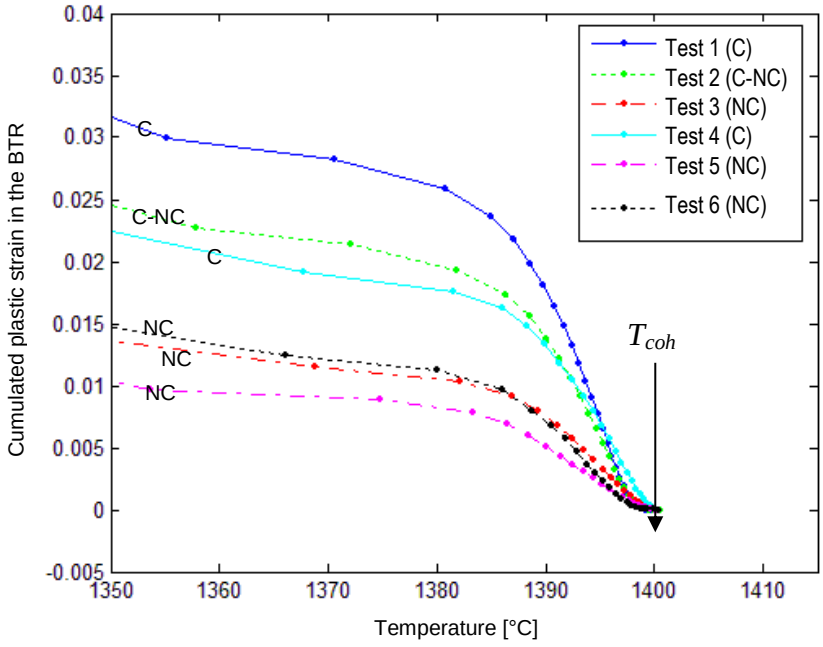

Figure 9: Calculated cumulated plastic strain as a function of temperature below the coherency temperature (1400 °C, f_s = 0.8) for the six tests studied.

6.2 Choice of coherency temperature

The coherency temperature T_{coh}, which is chosen as the upper bound of the BTR, is the temperature below which values of constitutive parameters start to increase, leading to increasing flow stress when temperature and liquid fraction decrease through the

solidification interval. Over this temperature, stresses are found at a very low level (significantly less than 1 MPa, as shown in Figure 7). Previous results have been obtained using a coherency temperature equal to 1400 °C, corresponding to a liquid fraction f_s = 0.80. The influence of the choice of this critical temperature has been tested, by choosing two other values: T_{coh} = 1415 °C (f_s = 0.60) and T_{coh} = 1392 °C (f_s = 0.85). Results are shown in Figure 10.

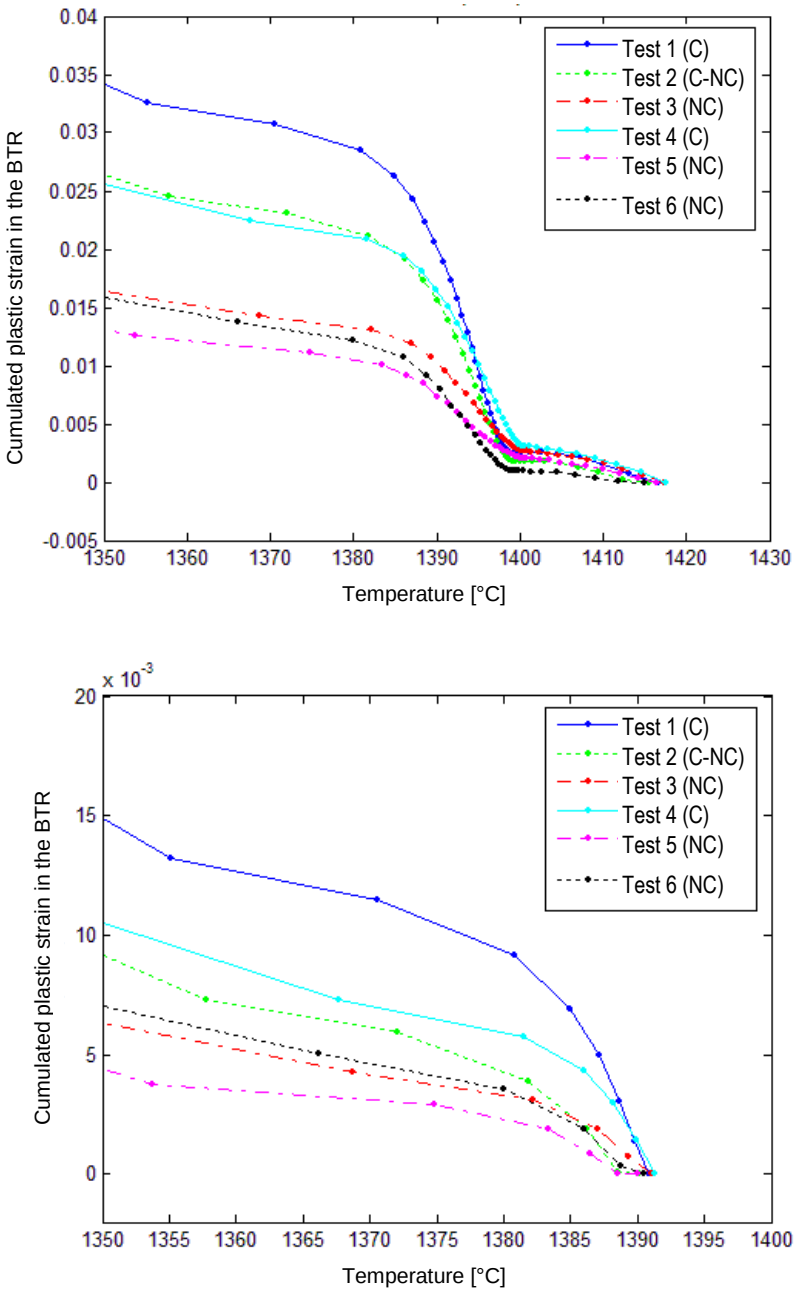

Figure 10: Influence of the choice of coherency temperature T_{coh} on the build-up of plastic strain. Top: T_{coh} = 1415 °C (f_s = 0.60), bottom: T_{coh} = 1392 °C (f_s = 0.85).

It can be seen that in those two additional calculations, the distinction between cracking and non-cracking tests is still possible. More precisely, when using a larger BTR (higher T_{coh}), the distinction is clear and the critical strain level is about the same as previously, around 0.015. However, when using a smaller BTR (lower T_{coh}), the distinction is not so clear and the critical strain level can be estimated around 0.0075, that is half the previous value.

Hence, the critical strain appears to be dependent of the extension of the BTR, which can be easily understood. In addition, it should be noted that such strains build-ups also depend on the definition of constitutive coefficients within the solidification interval, in a region where there is an evident lack of reliable data.

As a conclusion for the strain-based solid mechanics criterion, it has been found to provide an excellent discrimination between cracked and non-cracked specimens. The critical strain depends more on the choice of the upper bound of the BTR (coherency temperature) than on the choice of the lower bound (coalescence temperature). A critical value of 1.5% for the cumulated strain through the BTR defined between 1400 °C (f_s = 0.80) and 1360 °C (f_s = 0.95) appears appropriate. The effect of strain rate on the value of critical strain, previously mentioned by Won et al. (2000) and by Bellet et al. (2009), was not been studied, due to the restricted number of welding tests. That would require additional tests.

6.3 Interpretation through the RDG criterion

In view of applying the RDG criterion, a preliminary task consists in determining the different parameters involved in Eq. (4). The liquid viscosity μ is taken as 10^{-3} Pa s. The value of the secondary dendrite arm spacing λ_2 has been estimated, from SEM observations (see Section 3), to 7 μm. From data available in (Kerrouault, 2000), the shrinkage ratio β is taken as 0.086 and integrals A and B can be calculated as functions of the solidification path $f_s(T)$. Note that the bounds of the BTR used in Eq. (5) are the same as for the strain-based

criterion: T_{coh} = 1400 °C (f_s = 0.80) and T_{coal} = 1360 °C (f_s = 0.95). These material data are supplied in the first five columns of Table 3.

Table 3: Material and process parameters used in RDG criterion.

Secondary dendrite arm spacing λ_2 [µm]	Liquid viscosity [Pa s]	Shrinkage coefficient β	A [K]	B [K^2]	Strain rate [s^{-1}]	Norm of the thermal gradient G [K/mm]
7	0.001	0.086	4837	3054000	0.020 to 0.046	97 to 113

As for the process parameters, it can be noticed first that initiation of axial cracks at the rear of the mushy zone occurs in a quasi steady-state regime, during which the speed of the solidification front v_T can be considered equal to the welding speed V. The thermal gradient G has been estimated from the numerical calculations performed for the six test cases: its value has been found in the range 97 to 113 K/mm. Similarly the strain rate has been found in the range 0.020 to 0.046 s^{-1}. Those values are gathered in the last two columns of Table 3.

From Eq. (4), cracking should occur if

$$\Delta p_{crit} < \frac{180\mu}{G{\lambda_2}^2}\left[B\frac{(1+\beta)}{G}\dot{\varepsilon} + A\beta v_T \right] \tag{22}$$

On the basis of material and process parameters values of Table 3, the right hand side of this equation, which is the pressure drop undergone during welding, $\Delta p(G,\dot{\varepsilon})$, can be calculated for the six test cases. Results can be found in Table 4.

Table 4: Process parameters and calculated pressure drop for the six test cases.

Test #	Strain rate [s^{-1}]	Thermal gradient G [K/mm]	Pressure drop Δp [kPa]
1	0.046	97	133
2	0.040	106	106
3	0.023	113	81
4	0.030	109	96
5	0.020	111	84
6	0.027	103	105

Ranking now the tests from the lower to the higher pressure drops, we get Figure 11. It can be seen that there is a rather good agreement between calculated pressure drop and cracking occurrence. However, the correlation is not as good as for the strain-based criterion, due to test 4 for which a crack has formed despite a rather low calculated pressure drop: 96 kPa. From these results, it appears that the transition between cracking and non-cracking specimens would take place for calculated pressure drops in the range 90 to 120 kPa. A critical pressure drop value which could be retained to form a conservative RDG criterion (somewhat overestimating the cracking risk) would be $\Delta p_{crit} \approx 90$ kPa. This value is much higher than the value suggested by Rappaz et al. (1999) in their initial article: 2 kPa. However, it is of the same order as the limits determined experimentally by Wisniewski (2009) for copper alloys (50 kPa), and by Carlson et al. (2006) for aluminium alloys (160 kPa).

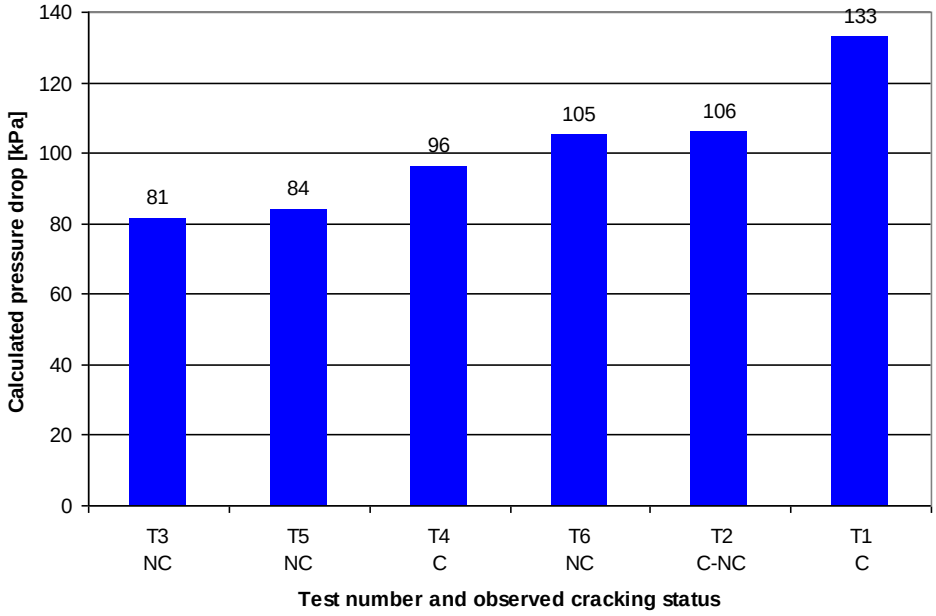

Figure 11: Comparison between calculated pressure drop and observed cracking status.

In view of such results, it is interesting to test the sensitivity of the calculated pressure drop values with respect to the different involved quantities. Supposing here that material data are known, our attention is focused on three other quantities: strain rate, thermal gradient and secondary dendrite arm spacing. The two first quantities are determined by analysis of the results of finite element modelling, whereas the last one is deduced either from Eq. (3), or from direct observation. From the expression of the pressure drop, Eq. (4), the following sensitivity coefficients can be derived:

$$\begin{cases} \dfrac{\partial(\Delta p)}{\partial \dot{\varepsilon}} = \dfrac{180\mu}{G^2 {\lambda_2}^2} B(1+\beta) \\ \dfrac{\partial(\Delta p)}{\partial G} = -\dfrac{180\mu}{G^2 {\lambda_2}^2}\left[2B\dfrac{(1+\beta)}{G}\dot{\varepsilon} + A\beta v_T \right] \\ \dfrac{\partial(\Delta p)}{\partial \lambda_2} = -2\dfrac{180\mu}{G {\lambda_2}^3}\left[B\dfrac{(1+\beta)}{G}\dot{\varepsilon} + A\beta v_T \right] \end{cases} \tag{23}$$

The average values of these sensitivity coefficients for the six test cases are the following:

$$\frac{\partial(\Delta p)}{\partial \dot{\varepsilon}} = 1083 \text{ kPa s} \qquad \frac{\partial(\Delta p)}{\partial G} = -1.29 \text{ kPa K}^{-1} \text{ mm} \qquad \frac{\partial(\Delta p)}{\partial \lambda_2} = -28.8 \text{ kPa } \mu\text{m}^{-1}$$

In Table 5 the impact of uncertainties on values of strain rate, thermal gradient and SDAS has been quantified, by choosing typical uncertainty values. It can be seen that effects of $\dot{\varepsilon}$ and G are limited. Conversely, the effect of SDAS is strikingly high. A small variation by 1 μm makes the pressure drop Δp vary considerably with respect to the critical value, previously identified around 90 kPa. This appears as a serious issue in the use of RDG criterion. Indeed, as neither formula such as Eq. (3), nor direct measurements can claim to be accurate enough, it is then extremely difficult to compare calculated pressure drops to a given critical threshold that would distinguish cracking and non-cracking states.

Table 5: Impact of uncertainties on calculated pressure drop.

Sensitivity coefficient	Average value (6 tests)	Estimated uncertainty on each variable			Impact on pressure drop Δp [kPa]
		$\Delta\dot{\varepsilon}$ [s^{-1}]	ΔG [K/mm]	$\Delta\lambda_2$ [μm]	
$\partial(\Delta p)/\partial\dot{\varepsilon}$	1083 kPa s	0.003	-	-	3.2
$\partial(\Delta p)/\partial G$	-1.29 kPa K^{-1} mm	-	3	-	-3.9
$\partial(\Delta p)/\partial\lambda_2$	-28.8 kPa μm^{-1}	-	-	1	-28.8

To summarize with the use of the RDG criterion, the consistency between calculated crack prediction and experimental observations is obtained at the price of a choice of a high value for the liquid cavitation pressure: 90 kPa. This value is among the highest ones found in the literature. Moreover, a sensitivity study has shown that the calculated pressure drop through the mushy zone – to be compared with this critical value – is dramatically dependent on the secondary dendrite arm spacing. This is an additional issue which might affect the predictability of this criterion.

In line with these last remarks, and before drawing final conclusions, it is worth drawing the attention on the fact that neither the critical strain threshold for the strain based criterion,

nor the pressure limit for the RDG criterion should be applied *stricto sensu* in thermomechanical analysis of welding for crack prediction. The reason for this is that the values that have been identified in the present study are obviously too dependent on the uncertainties regarding the thermomechanical response of the mushy zone, or its microstructural characteristics, especially the values of dendritic spacing, coherency temperature and the constitutive parameters around it. As such, the cracking criteria should be used as *hot cracking qualitative indicators* only, to serve in comparing different potential welding conditions and determine the best suited with respect to the risk of crack formation.

CONCLUSIONS

In this work, experimental and numerical analyses of solidification cracking in GTA welding of an austenitic stainless steel AISI 321 were carried out. After implementation of two crack criteria in the thermomechanical finite element modelling and comparison with experimental observations and measurements, the following conclusions could be drawn:

- The values of calculated internal stresses were not found discriminant between cracked and non-cracked specimens. This tends to exclude the use of stress-based crack criteria.
- The RDG criterion - based on the prediction of liquid cavitation as a precursor of crack opening - showed an acceptable ability to predict crack occurrence, at the price of a very high value (although steel admissible) for the liquid cavitation pressure.
- The best response in terms of cracking prediction was obtained with the strain-based solid mechanics criterion, using a critical value of 1.5% for the cumulated strain through the BTR defined between solid fractions 0.80 and 0.95.

REFERENCES

Bellet, M., Cerri, O., Bobadilla, M., Chastel, Y., 2009. Modeling of hot tearing during solidification of steels: assessment and improvement of macroscopic criteria through the analysis of two hot tearing tests. Metall. Mater. Trans. A 40, 2705-2717.

Campbell, J., 2003. Castings, second ed. Butterworth-Heinemann, Oxford, pp. 242-257.

Carlson, K.D., Lin, Z., Beckermann, C., Mazurkevich, G., Schneider, M.C., 2006. Modeling of porosity formation in aluminum alloys. In: Gandin, C.A., Bellet, M. (Eds.), Proceedings of 11th Int. Conf. on Modeling of Casting, Welding, and Advanced Solidification Processes, Opio, France, pp. 627-634.

Code_Aster, 2015. www.code-aster.org (last access date: 2015-07-16).

Cross, C.E., Boellinghaus, T., 2006. The effect of restraint on weld solidification cracking in aluminium. Welding in the World 50, 51-54.

Cross, C.E., Coniglio, N., 2008. Weld solidification cracking: critical conditions for crack initiation and growth. In: Böllinghaus, T., Herold, H., Cross, C.E., Lippold, J.C. (Eds.), Hot Cracking Phenomena in Welds II, Springer, pp. 47-66.

Eskin, D.G., Katgerman, L., 2007. A quest for a new hot tearing criterion. Metall. Mater. Trans. A 38, 1511-1519.

Farup, I., Rappaz, M., Drezet, J.M., 2001. In situ observation of hot tearing formation in succinonitrile-acetone. Acta Mater. 49, 1261-1269.

Kerrouault, N., 2000. Fissuration à chaud en soudage d'un acier inoxydable austénitique (Hot tearing during welding of an austenitic stainless steel). Ph.D. Thesis (in French), Ecole Centrale de Paris, also published as a technical report (CEA-R-5953, ISSN 0429 3460) by Commissariat à l'Energie Atomique, Saclay, France.

Kurz, W., Fisher, D.J., 1986. Fundamentals of Solidification. Trans Tech Publications, Switzerland.

Lahaie, D.J., Bouchard, M., 2001. Physical modeling of the deformation mechanisms of semisolid bodies and a mechanical criterion for hot tearing. Metall. Mater. Trans. B 32, 697-705.

Rappaz, M., Drezet, J.M., Gremaud, M., 1999. A new hot tearing criterion. Metall. Mater. Trans. A 30, 449-456.

Qiu, G., 2010. Etude de la modélisation de la fissuration à chaud en soudage d'un acier inoxydable austénitique (Study of hot tearing during welding of an austenitic stainless steel), Mines ParisTech, Paris, pp. 75-80.

Shibahara, M., Serizawa, H., Murakawa, H., 2001. Finite element method for hot cracking analysis using temperature dependent interface element. In: Cerjak, H. (Ed.) Proceedings of 5th Int. Conf. on Mathematical Modeling of Weld Phenomena, Graz, Austria, pp. 253-267.

Wisniewski, J., 2009. Modélisation thermomécanique de la fissuration à chaud en soudage par faisceau d'électrons d'un alliage CuCrZr (Thermo-mechanical modelling of hot tearing in electron beam welding of a CuCrZr alloy). Ph.D. Thesis (in French), University of Bretagne-Sud, Lorient, France, pp. 142-143.

Won, Y.M., Yeo, T.J., Seol, D.J., Oh, K.H., 2000. A new criterion for internal crack formation in continuously cast steels. Metall. Mater. Trans. B 31, 779-794.

Yamanaka, A., Nakajima, K., Yasumoto, K., Kawashima, H., Nakai, K., 1990. Measurement of critical strain for solidification cracking. In: Rappaz, M., Ozgu, M.R., Mahin, K.W. (Eds.), Proceedings of the 5th Int. Conf. on Modelling of Casting, Welding, and Advanced Solidification Processes, Davos, Switzerland, pp. 279-284.